

NUMERICAL MODELING OF LASER PRODUCED PLASMAS: THE DYNAMICS AND NEUTRON PRODUCTION IN DENSE SPHERICALLY SYMMETRIC PLASMAS

E. B. GOLDMAN

Laboratory for Laser Energetics, University of Rochester, Rochester, N.Y. 14627, U.S.A.

(Received 28 February 1972; and in revised form 23 May 1972)

Abstract—A series of numerical experiments have been conducted to investigate the dynamics and neutron production in laser irradiated, dense spherically symmetric plasmas. The results have led to the development of scalings for energy absorption, shock strength and optimum neutron production for sub-nanosecond, high energy pulses.

1. INTRODUCTION

THE POSSIBILITY of using high power pulsed lasers to initiate fusion reactions in dense plasmas has stimulated great interest in their dynamics. We have conducted a series of numerical experiments to investigate the dynamics and neutron production in laser irradiated, dense, spherically symmetric plasmas. In particular, we are interested in developing scalings for the absorbed energy, the shock strength and the neutron production.

A dense plasma can be described by the hydrodynamic and phenomenological equations set forth in Section 2. These are incorporated in a numerical model, developed into the LPP-1 computer code (GOLDMAN, 1971), which includes classical absorption (DAWSON and OBERMAN, 1962), a relativistic correction and cut-off in an overdense plasma (KAW and DAWSON, 1969), separate species temperatures, and molecular heat transport. Fluid-in-Cell methods (GENTRY *et al.*, 1966), suitably modified for two temperature plasmas with implicit treatment of the energy terms, are used to integrate the model equations.

Our work differs in a number of significant aspects from the few previous numerical investigations of spherical laser plasmas. There is no *a priori* constraint on the density and velocity profiles as imposed on the similarity models (HAUGHT and POLK, 1970; LUBIN *et al.*, 1971). The LPP-1 code allows for arbitrary initial conditions which we have taken to be a cold plasma at rest with a dense inner core surrounded by a low density tail (the exact specifications are given in Section 3). Other Lagrangian codes have been used to examine the result of plasma irradiation by low power lasers for comparison with specific experiments (FADER, 1968; MEAD, 1970). Since there is no attempt to reproduce experimental data here, we are free to examine more energetic pulses and obtain a richer set of results.

Section 3 contains a discussion of the plasma dynamics and Section 4 contains the results of 30 numerical experiments with different size plasmas and different laser powers (all experiments were run with 10 psec rise time pulses). Two important observations are made. The first is that once part of the laser energy absorbed by the tail electrons has been transported into the dense core, a spherically converging heat front is formed. In accordance with the theory of non-linear heat conduction, the front may or may not transform into an imploding shock depending on the

amount of electron thermal energy behind it. The dynamics of the plasma and its neutron production differ greatly under these two possibilities. A second observation is that a graph of total neutron production as a function of the absorbed energy shows a peak in that portion of the curve which represents shock cases.

In Section 5 we develop a scaling to predict the amount of absorption in a given plasma, and in Section 6 we develop a model to predict neutron production as a function of the imploding shock speed. Section 7 is an analysis of shock wave formation which uses the model of Section 6 to explain the results in Section 4. The final section contains a scaling for the shock wave speed and the absorbed energy. Combining these results, the scaling of Section 5 gives the absorbed energy, that of Section 8 the shock speed and the model of Section 6 the neutron production for a specified plasma and laser pulse.

2. THE PLASMA MODEL

We assume that we are working with a fully ionized, quasi-neutral two temperature plasma whose components are perfect gases. The ions (singly charged) and the electrons will have the same number density n and the same velocity u so that only a single momentum equation is required (GOLDMAN, 1971)

$$\rho \frac{\partial u}{\partial t} + \rho u \frac{\partial u}{\partial r} + \frac{\partial p}{\partial r} = 0 \quad (1)$$

where

$$\rho = (m^+ + m^-)n, \quad p = nk(T^+ + T^-) \quad (2)$$

and m^\pm and T^\pm are the masses and temperatures of the ions and electrons. Two individual energy equations account for the separate species temperatures

$$m^-n \frac{\partial e^-}{\partial t} + m^-nu \frac{\partial e^-}{\partial r} + nkT^- \frac{\partial u}{\partial r} = \frac{1}{r^2} \frac{\partial}{\partial r} \left[\kappa^- r^2 \frac{\partial T^-}{\partial r} \right] - \frac{3}{2}kn(T^- - T^+) \tau^{-1} + W \quad (3)$$

$$m^+n \frac{\partial e^+}{\partial t} + m^+nu \frac{\partial e^+}{\partial r} + nkT^+ \frac{\partial u}{\partial r} = \frac{1}{r^2} \frac{\partial}{\partial r} \left[\kappa^+ r^2 \frac{\partial T^+}{\partial r} \right] + \frac{3}{2}kn(T^- - T^+) \tau^{-1}. \quad (4)$$

Taking the ratio of specific heats to have a constant value of $\frac{5}{3}$, we can write the energies in terms of the temperatures as

$$e^\pm = \frac{5}{2}kT^\pm/m^\pm. \quad (5)$$

Viscosity does not contribute to the evolution of the plasma except in the very narrow region of the shock or thermal front. Since this contribution is essentially negligible compared to other effects, true viscous terms are omitted in favor of a pseudo-viscous pressure of the type used by GENTRY *et al.* (1966) in the numerical computation. The evolution is dominated by the thermal effects; laser heating, electron heat conduction, and the energy transfer between species (also referred to as temperature relaxation).

W is the rate at which energy is absorbed by the plasma

$$W(r, t) = P_0 \phi(t) \left\{ 1 - \exp \left[- \int_{r_0(t)}^r \kappa(r', t) dr' \right] \right\} \quad (6)$$

$P_0\phi(t)$ is the power profile of the laser pulse where $\phi(t)$ is the modified Gaussian

$$\phi(t) = \begin{cases} 1.9t/t_r & t/t_r < 0.455 \\ \exp[-(1 - t/t_r)^2/2.0164] & 0.455 \leq t/t_r \leq 1 \\ \exp[-(1 - t/t_r)^2] & 1 < t/t_r \leq 2 \\ 0 & t/t_r > 2 \end{cases} \quad (7)$$

t_r , the rise time, is the half-width of the pulse and is the only parameter necessary to specify $\phi(t)$ as shown in Fig. 1. Since little energy would be absorbed from a pulse continuing beyond two rise times, we have assumed a cut-off at this point in order to reduce the computation time needed for each case. $r_*(t)$ is the outer radius of the plasma and $\kappa(r, t)$ is the absorption coefficient (DAWSON and OBERMAN, 1962)

$$\kappa(r, t) = 8\pi e^6 \ln \Lambda n^2 (3c\omega_i^2)^{-1} (2\pi m^- kT^-)^{-3/2} (1 - \omega_{pe}^2/\omega_i^2)^{-1/2} \quad (8)$$

where c and ω_i are the speed of light and the laser frequency ($1.78 \times 10^{15} \text{ sec}^{-1}$) and $\ln \Lambda$ is the coulomb logarithm. The effective plasma frequency, ω_{pe} , depends on the classical plasma frequency and the local laser intensity $I(r, t)$ as expressed by the relativistic correction (KAW and DAWSON, 1969)

$$\begin{aligned} \omega_{pe}^2 &= \omega_p^2 [1 - 377I(r, t)(e/m^-c)^2]^{-1} \\ \omega_p^2 &= 4\pi e^2 n/m^-. \end{aligned} \quad (9)$$

The thermal conductivities can be expressed directly in terms of the temperatures as (DAWSON, 1964)

$$\begin{aligned} \kappa^- &= 1.27 \times 10^{-4} (T^-)^{5/2} \\ \kappa^+ &= 2.96 \times 10^{-6} (T^+)^{5/2} \end{aligned} \quad (10)$$

(all units in this paper are in c.g.s. with temperatures in $^\circ\text{K}$), while energy transfer depends on the relaxation time

$$\tau = 53.1 n^{-1} (T^-)^{3/2}. \quad (11)$$

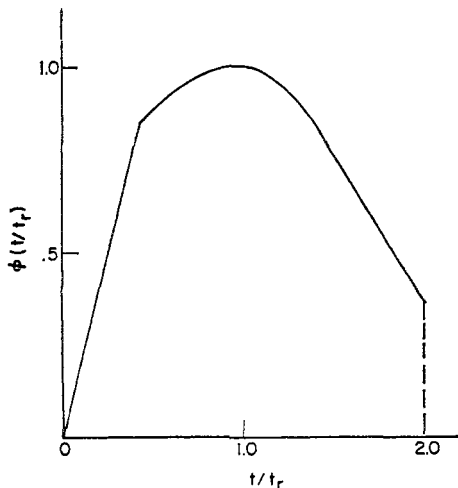


FIG. 1.—The pulse shape $\phi(t)$ as a function of normalized time t/t_r .

In order to study the fundamental dynamics of the plasma, several interesting plasma effects and laser-plasma interactions have been omitted (indeed, some of these cannot be modeled in a one-dimensional code). These include the electromagnetic stresses and self-focusing, non-linear coupling and anomalous absorption, recombination, and thermoelectric effects. Alpha particle heating and Bremsstrahlung losses are negligible compared to the plasma energy densities considered here, and these have also been omitted.

We have restricted our attention to a spherically symmetric plasma where all variables are functions of time and the radial coordinate only. The computational space is divided into concentric shells of thickness Δr to which we apply a two-temperature, one-dimensional version of the Fluid-in-Cell model of GENTRY (1966). In this mixed Euler-Lagrangian scheme, all variables are first advanced in time using finite difference analogues of the momentum and energy equations. Central differences for spacial derivatives are referred to the Eulerian grid of concentric shells, and the transport terms, $u(\partial/\partial r)$, are omitted completely at this step. Later, these terms and the missing continuity equation are accounted for by the Lagrangian transport of fluid across shell boundaries.

This computational scheme plus a number of specialized techniques have been incorporated into the computer code LPP-1 to create a numerical model of a freely disassembling, laser produced plasma. The complete details of this model, including the selection of space and time steps, can be found in GOLDMAN (1971). As noted there, it is possible to develop two codes, one for explicit and one for implicit handling of heat conduction—the choice depending on the step size selected and the peak electron temperatures anticipated (see Fig. 1 of GOLDMAN (1971) and the related discussion). Here, we use the fully implicit code.

3. PLASMA DYNAMICS

A prepulse from the laser converts a pellet of frozen deuterium into a spherical, fully ionized plasma with the density profile in Fig. 2 (see LEISING *et al.* (1972) for a discussion of prepulse vaporization of solid targets). It is convenient to normalize the density to n_0 , the number density of the deuterium ice ($n_0 = 4 \times 10^{22} \text{ cm}^{-3}$). The profile consists of a high density core of radius r_c surrounded by a low density tail of thickness r_t . We specify the plasma by referring to these two radii, e.g. a 100 μ /100 μ plasma is one with a 100 μ radius core surrounded by a 100 μ tail for a total radius, r_0 , of 200 μ .

A low density tail is necessary to promote energy absorption from the laser which is assumed to uniformly illuminate the surface of the plasma. For laser intensities below 10^{17} W/cm^2 and a laser wavelength of $1.06 \times 10^4 \text{ \AA}$, equations (8) and (9) indicate that there can be no absorption for normalized plasma densities greater than 0.0248. In the plasmas considered here, the tail is specified to have the parabolic profile such that

$$\begin{aligned} n(r_c)/n_0 &= 0.0248 \\ n(r_0)/n_0 &= 0.00248 \\ dn/dr &= 0 \quad r = r_0. \end{aligned} \tag{12}$$

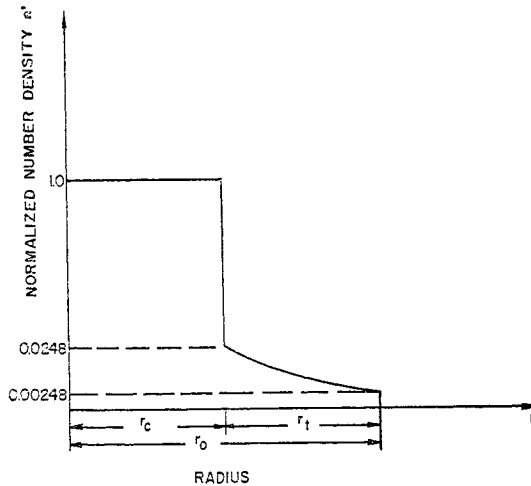


FIG. 2.—Sketch of the initial normalized density profile as a function of radius. The core radius, r_c , plasma radius r_0 , and tail thickness r_t have been indicated.

Normally, reflection from the discontinuity at $r = r_0$ should be taken into account; however, we assume that the plasma density disappears smoothly between r_0 and $r_0 + \Delta r$, and this behavior cannot be resolved on the finite difference grid.

Plasma electrons absorb energy from the laser by inverse Bremsstrahlung, but this radiation can propagate only as long as the laser frequency is greater than the local plasma frequency. Absorption is enhanced when the electrons are driven to velocities near the speed of light where the relativistic correction in equation (9) shows a decrease in the local effective plasma frequency. Very large increases in absorption can occur when the electron density is just slightly less than the cut-off in equation (8). On the finite difference grid, complete reflection occurs at the outer surface of the first overdense shell and there is a possibility that additional energy may be absorbed from the reflected beam.

When the electrons in the tail have been heated to 10^6 – 10^7 °K, the ability of the plasma to absorb more energy decreases rapidly. However, the tail does not become completely transparent to the radiation, i.e., reduced absorption does continue to two rise times because part of the electron thermal energy is steadily drained away by collisions with the cold ions, by transformation into kinetic energy and by thermal transport into the high density core.

The energy in the electron thermal mode within the core drives an imploding spherical heat front. We can estimate the velocity of this front at any instant by considering electron thermal transport. The energy transported across unit area in unit time at a velocity V_T is $\frac{3}{2}nkT^-V_T$. Equating this to the thermal transport, $\lambda(\partial T^-/\partial r)$, where $\lambda = \hat{C}(T^-)^{5/2}$ is the electron thermal conductivity, gives

$$V_T = \frac{3}{2} \hat{C}(T^-)^{3/2} \frac{\partial T^-}{\partial r} / nk \quad (13)$$

and we now take V_T as measure of the frontal velocity where T^- and $\partial T^-/\partial r$ are measures of the electron temperature and its gradient at the front.

A local velocity gradient is established by the temperature gradient in the thermal front. This velocity gradient will, in turn, establish a density perturbation which

can be estimated from the mixture continuity equation

$$\frac{\partial \rho}{\partial t} + u \frac{\partial \rho}{\partial r} = -\rho \frac{\partial(ur)^2}{\partial r} / r^2. \quad (14)$$

Integrating along a particle path,

$$\rho \simeq \exp \left[- \int_{r^*}^r \frac{\partial u}{\partial r} dt \right] \quad (15)$$

where ρ and u are the density and velocity of the ion-electron mixture ($\partial u/\partial r$ is negative). Both $\partial u/\partial r$ and $\partial T^-/\partial r$ will be non-zero only over some length l_f , which is a measure of the width of the thermal front. If \bar{U} is a measure of the velocity imparted to the mixture behind the front, then from (15), $(\bar{U}/l_f)^{-1}$ is a measure of the time necessary to establish a density perturbation. $(V_T/l_f)^{-1}$ is a measure of the time required for the passage of the thermal front and the time for which the gradients are non-zero at a given point. If $V_T > \bar{U}$, no perturbations can form.

\bar{U} can be estimated from the momentum equation (1)

$$\frac{\partial u}{\partial t} + u \frac{\partial u}{\partial r} = -R \frac{\partial T}{\partial r} \quad (16)$$

from which viscosity and density gradients have been omitted. R is the mixture gas constant and T the mixture temperature $T = (T^+ + T^-)/2 \simeq T^-/2$ (the ions at the front are cold). Integrating from rest following a particle and again using the fact that $\partial T^-/\partial r$ is non-zero only over l_f ,

$$\bar{U} \simeq R l_f \frac{\partial T}{\partial r} / V_T. \quad (17)$$

If $\partial T^-/\partial r \simeq T^-/l_f$, the thermal frontal velocity and the velocity behind the front can coincide only at the isothermal mixture acoustic velocity

$$U_a = (RT)^{1/2} \quad (18)$$

A thermal front can therefore exist only as long as there is sufficient energy behind it to maintain $V_T > U_a$ and this type of behavior occurs only in media with non-linear thermal conductivities (ZELDOVICH and RAIZER, 1966). When the frontal velocity has become acoustic, the density perturbation can amplify, and a converging hydrodynamic shock front forms. The transition from thermal to shock behavior can be estimated from (13) and (18)

$$V_T/U_a = [\frac{2}{3} \hat{C} / nk(R/2)^{1/2} l_f] (T^-)^2 = 3.38 \times 10^{-15} (T^-)^2 \quad (19)$$

where we have used T^-/l_f as a measure of $\partial T^-/\partial r$ and have set $l_f = 5 \mu$ and $n = n_0$. Electron temperatures on the order of 2×10^7 °K are required to maintain these thermal fronts.

Assuming a uniform temperature distribution throughout a 100μ core, this result requires that 72.8 J be in the electron thermal mode if the thermal front is to reach the center of the plasma. If 70 per cent of the absorbed energy (see Table 1, column 7) is contained in the thermal mode, then for absorbed energies greater than 104 J, no shocks will form. This figure compares favorably with the results of the next section.

TABLE 1.—SUMMARY OF DATA FOR 30 EXPERIMENTAL CASES. T.D. DENOTES A THERMALLY DOMINATED CASE, * A CASE RUN ONLY TO OBTAIN A POINT ON THE ABSORPTION CURVE FIG. 9 AND ** A CASE RUN ONLY TO OBTAIN A POINT ON THE SHOCK SPEED PARAMETER CURVES FIGS. 14 AND 17

Case #	r_c/r_t μ/μ	P_0 Watts	E Joules	E_a Joules	$\frac{100E_a}{E}$	$\frac{\%E_a \text{ in}}{\text{Thermal mode}}$	ξ m/sec $^{\bar{n}}$	# Neutrons produced
1	100/50	1.52×10^{14}	2008	32.3	1.61	62.0	273.8	3.2×10^6
2	100/50	7.5×10^{14}	9950	116.4	1.17	74.1	*	
3	100/100	1.0×10^{13}	132	10.7	8.07	36.7	165.7	2.0×10^8
4	100/100	3.3×10^{13}	437	20.1	4.76	48.5	227.5	1.9×10^5
5	100/100	5.0×10^{13}	662	26.8	4.04	52.9	248.5	1.1×10^6
6	100/100	1.0×10^{14}	1321	40.0	3.03	58.8	297.4	7.9×10^6
7	100/100	1.25×10^{14}	1655	46.5	2.81	61.0	305.4	**
8	100/100	1.5×10^{14}	1990	50.5	2.54	61.9	319.6	2.1×10^7
9	100/100	2.25×10^{14}	2985	66.0	2.21	64.6	341.5	**
10	100/100	2.6×10^{14}	3446	73.1	2.12	66.5	346.4	**
11	100/100	3.0×10^{14}	3971	89.7	1.96	68.7	345.1	6.9×10^7
12	100/100	4.5×10^{14}	5961	101.8	1.71	69.7	343.6	6.9×10^7
13	100/100	6×10^{14}	7951	134.4	1.69	72.3	T.D.	5.2×10^7
14	100/100	7.7×10^{14}	10221	160.5	1.57	73.4	*	
15	100/100	9.0×10^{14}	11940	177.6	1.49	73.8	T.D.	2.7×10^7
16	100/100	1.0×10^{15}	13206	191.5	1.45	73.9	*	
17	100/100	1.2×10^{15}	15900	208.5	1.31	74.3	T.D.	1.8×10^7
18	200/100	1.21×10^{15}	16100	328.4	2.04	72.3	381.1	**
19	200/100	3.0×10^{15}	39708	706.8	1.78	78.8	451.8	**
20	200/100	6.0×10^{15}	79507	1296.0	1.63	82.1	451.9	**
21	200/200	8.0×10^{14}	10583	426.5	4.03	66.4	391.3	3.9×10^8
22	200/200	2.0×10^{15}	26503	771.2	2.91	72.2	468.1	**
23	200/200	2.6×10^{15}	34462	927.0	2.69	74.3	481.9	3.7×10^8
24	200/200	2.9×10^{15}	38442	1026.4	2.67	75.4	479.4	**
25	200/200	3.8×10^{15}	50291	1191.9	2.37	76.8	469.8	3.6×10^8
26	300/300	2.7×10^{15}	35729	771.2	4.69	69.2	483.4	**
27	300/300	9.16×10^{15}	121206	3733.1	3.08	77.3	562.0	**
28	300/300	1.0×10^{16}	132060	3961.8	3.00	77.3	569.7	**
29	300/300	1.13×10^{16}	149246	4522.2	3.03	78.6	573.1	**
30	300/300	1.3×10^{16}	171859	4880.8	2.84	79.0	565.3	4.1×10^{10}

4. THE NUMERICAL EXPERIMENT

We have used the fully implicit version of the LPP-1 code to perform the series of numerical experiments listed in Table 1. The second column is the plasma specification, P_0 is the peak power in watts, and E is the total laser energy in the cut-off modified Gaussian pulse in joules. All of the cases are for a rise time of 10 psec.

Assuming that a prepulse has established the density distribution of equation (12), we turn on the main pulse of Fig. 1 at $t = 0$ and begin heating the tail electrons as described in the previous section. It was noted there that when the electrons in the tail have been heated to 10^6 – 10^7 °K, the ability of the plasma to absorb more energy decreases rapidly. Figure 3 shows the percent absorption of energy from the laser as a function of time, and the net energy absorbed, E_a , and the percent net energy absorbed, $100E_a/E$ are shown in Table 1. For plasmas with the same ratio of tail thickness to core radius, a scaling can be developed to predict E_a as discussed in the next section. We note that the amount of energy absorbed can probably be optimized by pulse tailoring, but such considerations are beyond the scope of this paper.

Transfer of energy to the cold ions, transformation of thermal energy into kinetic energy of expansion and transport of energy into the electrons within the core allow

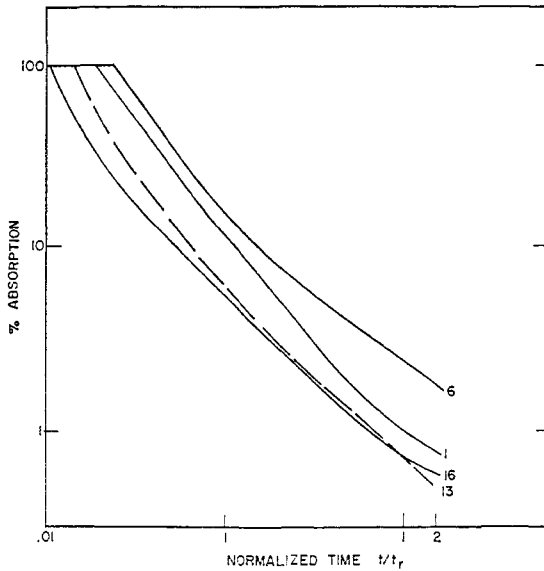


FIG. 3.—Per cent absorption as a function of normalized time, t/t_r , for 4 cases. (Case 13 is shown by a broken line for clarity only.)

the absorption process in the tail to continue as long as the laser is switched on. An investigation of the state of the plasma at two rise times reveals that most of the absorbed energy is now in the electron thermal mode in the core. Since the original interface between the core and the tail becomes somewhat diffuse, the core is redefined as all of the plasma within a radius r_c of the center, regardless of its density. The percentage of the absorbed energy in the core electron thermal mode is listed in the seventh column of Table 1.

The energy in the core electrons drives the imploding spherical front. When the frontal velocity has become sonic, the density perturbations become pronounced and a converging hydrodynamic shock wave forms. Convergence effects strengthen the shock and its velocity eventually becomes compression limited. Any case for which the compression ratio (density ahead of the shock to the maximum density) reaches a value of 4 before the shock reaches the center is referred to as shock dominated. The density and temperature profiles for a representative shock dominated case, no. 3, are shown in Figs. 4 and 5 at 20, 100 and 560 psec, (a slight numerical instability has been smoothed out of the ion temperature curves near $r = 100 \mu$ at 20 and 100 psec). Here the thermal front rapidly transformed into a shock front strengthened by both convergence and the temperature gradient. Behavior typical of the shock dominated cases can be seen in the temperature profiles at 100 psec; the ions and the electrons are heated to the same temperature by the shock while the electrons behind the shock are further heated by laser energy carried by electron thermal transport (the inflection in the curve is a convergence effect). In this particular case, so little energy was available and the shock velocity was so low that the plasma became one temperature at 450 psec. Other shock dominated cases at higher energies continue to show two temperatures behind the front until it collapses at the center.

Collapse of the shock wave on the center causes large increases in density and temperature. These peaks decay rapidly as the expansion which has been following

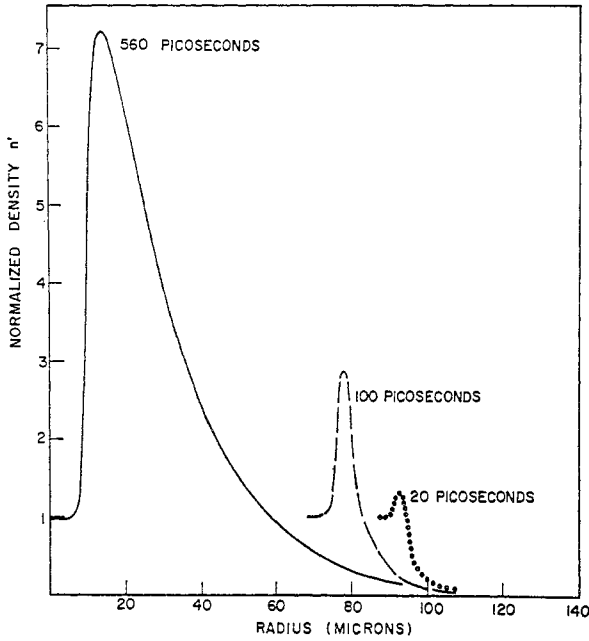


FIG. 4.—Normalized density distribution as a function of radius for case #3 at 20, 100 and 560 psec.

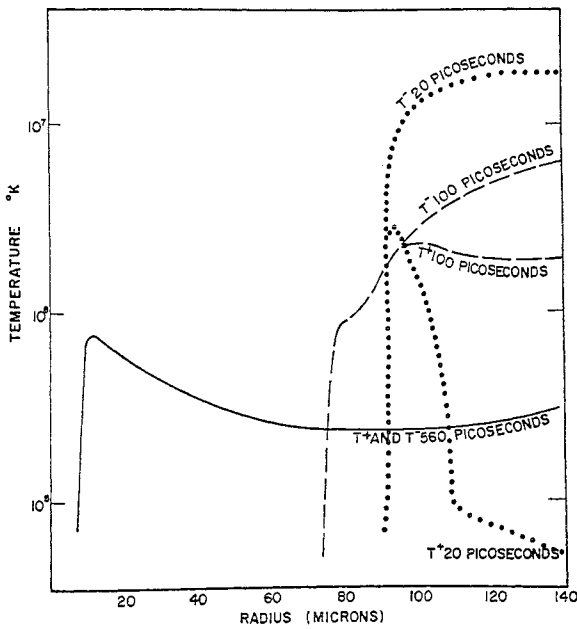


FIG. 5.—Electron (T^-) and ion (T^+) temperature distributions as a function of radius for case #3 at 20, 100 and 560 psec.

both the thermal and shock fronts gains the center, and, from this point, the plasma cools rapidly with relatively uniform temperatures. The total neutron production to time t is given by

$$N = \int_{\text{vol}} \int_0^t \frac{1}{2} n^2 \langle \sigma V \rangle_{\text{ave}} dt d\text{vol} \quad (20)$$

where σ is a reaction cross section and V the relative velocity of approach. For a Maxwellian distribution of ion velocities about a temperature T^+ and deuterium-deuterium reactions this becomes (ARTSIMOVICH, 1964)

$$N = 1.3 \times 10^{-14} \int_{\text{vol}} \int_0^t n^2 \left(\frac{1.1605 \times 10^7}{T^+} \right)^{2/3} \times \exp \left[-18.76 \times \left(\frac{1.1605 \times 10^7}{T^+} \right)^{1/3} \right] dt d\text{vol} \quad (21)$$

N is shown as a function of t in Fig. 6 for case no. 12. The jump in the curve coincides with the collapse of the shock on the center.

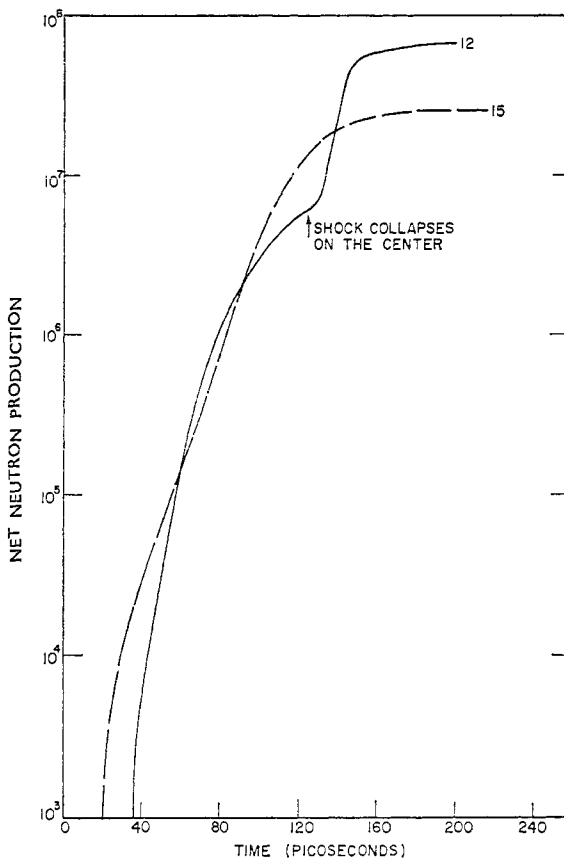


FIG. 6.—Net neutron production as a function of time for the shock dominated case #12 and the thermally dominated case #15.

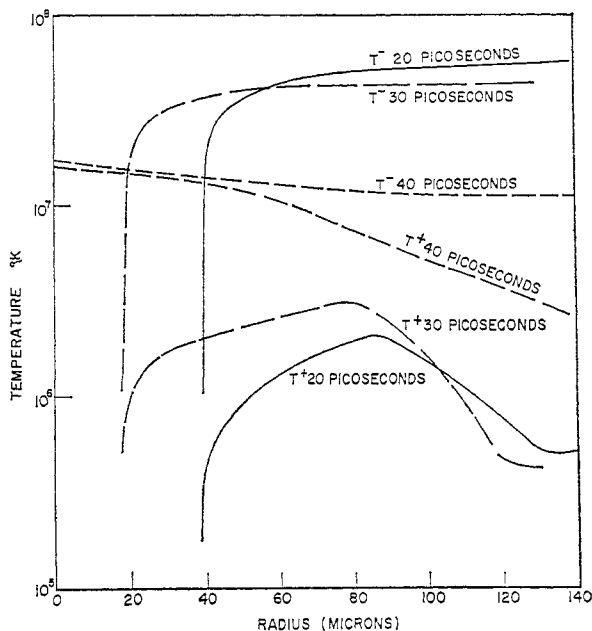


FIG. 7.—Electron (T^-) and ion (T^+) temperature distributions as a function of radius for case #15 at 20, 30 and 40 psec.

If the energy densities are high enough, either no shock will form or if one does, it will not reach full strength (i.e. density ratio ≥ 4) before collapse. We refer to these as thermally dominated cases. The temperature profiles for case no. 15, which is typical of those with no shock formation, are shown in Fig. 7 at 20, 30 and 40 psec. Note that the electron temperatures remain above those estimated in the last section to be required for maintenance of a thermal front. Here the electrons are heated only by thermal transport of energy from the laser and the ions only by the slow (compared with the transit time of the front) process of ion-electron collisional transfer. Energy equilibration between the species is poor until the convergence effects at the center can create a moderate density enhancement which aids the exchange process as seen from equation (11). A smoother neutron production curve is found in the thermally dominated cases as shown in Fig. 6 for case 15.

A plot of neutron production vs absorbed energy is shown in Fig. 8 for the 100μ core plasmas. The maximum in the curve occurs at about 80 J while the transition from shock dominated to thermally dominated cases occurs at about 108 J as predicted in the last section. In order to understand this result, we have developed a simple model of neutron production in the shock dominated cases. This is presented in Section 6. The analysis of the behavior of the thermal and shock fronts and the transition from one to the other is given in Section 7 and these results along with those of Section 6 are used to interpret the last figure. An additional scaling is discussed in Section 8.

5. ABSORPTION

We can derive a simple expression to relate the amount of absorption in two plasmas with the same ratio of core radius to tail thickness. In any plasma, the

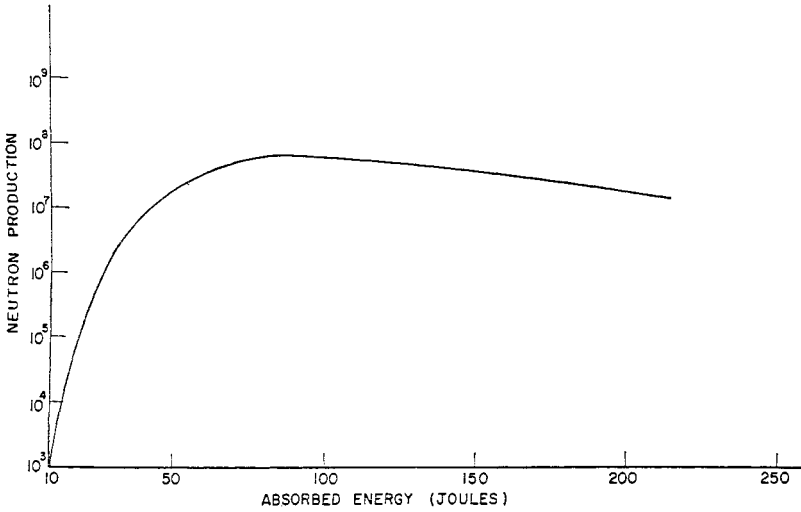


FIG. 8.—Neutron production as a function of absorbed energy for cases with a 100 μ radius core.

energy that can be placed in the thermal mode of the tail electrons is limited by transparency at high temperatures. Except for the earliest stages of heating, the electrons exist in a state where further absorption is possible only if some of their thermal energy is siphoned off by ion collisions, transformation into kinetic energy or transport into the dense, non-absorbing core. Further absorption then maintains the level of thermal energy against depletion. Since the energy level varies with the current input, we express these conditions as

$$4\pi \int_{r_c}^{r_0} r^2 n(r, t) \left[\frac{3}{2} k T^-(r, t) \right] dr \propto E \left[1 - \exp \left\{ -2\bar{\kappa} \int_{r_c}^{r_0} n^2(r, t) [T^-(r, t)]^{-3/2} \left[1 - \frac{4\pi e^2}{m^- \omega_i^2} n(r, t) \right]^{-1/2} dr \right\} \right] \quad (22)$$

where $n(r, t)$ and $T^-(r, t)$ are the electron density and temperature profiles in the tail $r_c \leq r \leq r_0$, and the absorption coefficient of equation (8) is rewritten as

$$\kappa(r, t) = \bar{\kappa} n^2(r, t) [T^-(r, t)]^{-3/2} \left[1 - \frac{4\pi e^2}{m^- \omega_i^2} n(r, t) \right]^{-1/2} \quad (23)$$

(the factor of 2 accounts for reflection). The relativistic correction has been eliminated from (15) because of the relatively low intensities considered here. It is convenient to non-dimensionalize the radial coordinate

$$r' = r/r_0, \quad r'_c = r_c/r_0 \quad (24)$$

so equation (22) becomes

$$6\pi k r_0^3 \int_{r'_c}^1 r'^2 n T^- dr' \propto E \left[1 - \exp \left\{ -2\bar{\kappa} r_0 \int_{r'_c}^1 n^2 (T^-)^{-3/2} \left[1 - \frac{4\pi n e^2}{\omega_i^2 m^-} \right]^{-1/2} dr' \right\} \right] \quad (25)$$

The time scale for the transport of energy by electron thermal transport within the tail is (DAWSON, 1964)

$$\tau_{hc} = 1.57 \times 10^{-10} (r_0 - r_c)^2 n (T^-)^{-5/2}. \quad (26)$$

For a density of $0.02n_0$, a temperature of 2.2×10^7 °K and $(r_0 - r_c) = 0.01$ cm, $\tau_{hc} \simeq 4.5$ psec and we therefore assume the electron temperature to be uniform through the tail and varying with time only. Similarly, since the maximum observed velocities during the first two rise times are on the order of 10^6 cm/sec, no part of the plasma can be displaced more than 0.1μ , and we treat the initial density profile as stationary in time.

Figure 3 illustrates the rapid decrease of absorption of laser energy in four cases. Although most of the laser energy is contained in the pulse between $0.455 t_r$ and $2 t_r$ (see Fig. 1), only a small percentage is being absorbed for $t \geq 0.455 t_r$. The exponential in equation (25) can be expanded for small values to yield

$$6\pi k T^-(t) \int_{r_c}^1 r'^2 n(r') dr' \propto \frac{E}{r_0^3} 2\bar{\kappa} r_0 T^-(t)^{-3/2} \int_{r_c}^1 n^2(r) \left[1 - \frac{4\pi r'^2 n(r')}{m^- \omega_l^2} \right]^{-1/2} dr'. \quad (27)$$

This equation will give incorrect results for the early stage of heating, but the total amounts of energy absorbed there are small and do not contribute significantly to the final total.

Consider two plasmas with radii r_{01} and r_{02} . Let $r_{c1}/r_{01} = r_{c2}/r_{02}$, which implies equal values for the corresponding integrals from equation (27), and let $T_1^-(t)$ and $T_2^-(t)$ be the uniform electron tail temperatures. Writing equation (27) for each of these plasmas and dividing, we obtain

$$[T_2^-(t)/T_1^-(t)]^{5/2} = \frac{r_{02} E_2/r_{02}^3}{r_{01} E_1/r_{01}^3}. \quad (28)$$

If E_1 and E_2 are in the proportion $r_{01}^3:r_{02}^3$, then

$$T_2^-(t)/T_1^-(t) = (r_{02}/r_{01})^{2/5}. \quad (29)$$

Since (29) must hold at each instant of time (again excepting the very early stages of heating), it follows that

$$\frac{\% \text{ absorption in plasma 2}}{\% \text{ absorption in plasma 1}} = \left(\frac{r_{02}}{r_{01}} \right)^{2/5}. \quad (30)$$

We have used the percent net absorption in the $100 \mu/100 \mu$ plasmas to construct the curve in Fig. 9 and the other cases with $r_c/r_t = 1$ have been displayed as numbered points. The $200 \mu/200 \mu$ and $300 \mu/300 \mu$ cases, with energies and per cent absorptions reduced by 2^{-3} , 3^{-3} , $2^{-0.4}$ and $3^{-0.4}$ respectively, are in excellent agreement with the $100 \mu/100 \mu$ curve. We did not run enough cases to determine a $100 \mu/50 \mu$ base curve, but reduction of the energies and per cent absorptions of cases 18 and 20 by 2^{-3} and $2^{-0.4}$ gives good agreement with the corresponding quantities of cases 1 and 2.

These results allow us to compute the percent absorption in a plasma given the experimentally determined base curve. The results obtained in this section depend directly on the classical description of the absorption process that has been incorporated into the numerical model. In the following sections, the discussion will be seen to depend on the magnitude of the absorbed energy. While the dependency of E_a on E will vary with the description of absorption, such changes cannot influence results stated in terms of E_a .

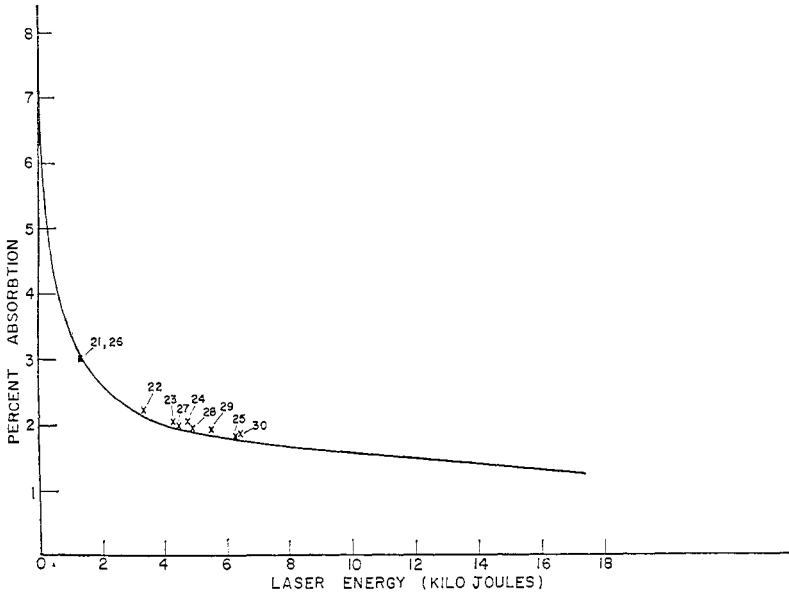


FIG. 9.—Per cent absorption as a function of the laser energy. The solid line is constructed from the $100\ \mu/100\ \mu$ cases while the reduced values for $200\ \mu/200\ \mu$, and $300\ \mu/300\ \mu$ cases are shown as numbered crosses.

6. NEUTRON PRODUCTION MODEL

The results in Section 4 indicate that neutron production is stimulated by the collapse of the shock on the center (see Fig. 6). In this section, we idealize the behavior of the imploding shock wave and follow its dynamics by reconstructing the analysis of GUDERLY (1942). A model of neutron production is constructed from the resulting time histories of the pressure and densities through the incorporation of equation (21).

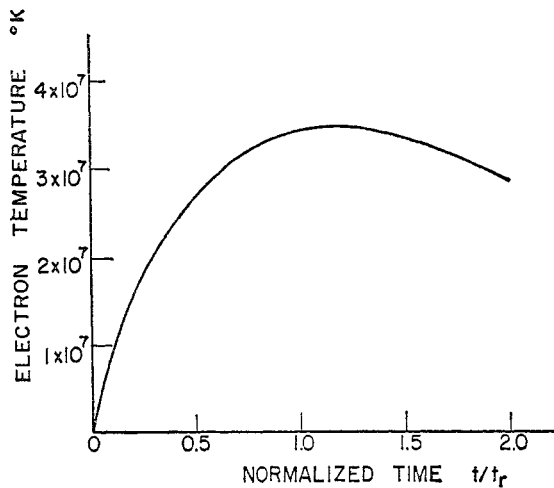


FIG. 10.—Electron temperature as a function of normalized time for the tail in case 6.

Every spherical shock wave is characterized by a number ξ , the shock speed parameter, which is a measure of its potential amplification by convergence. For sufficiently small radius, the trajectory of the front is expressed as

$$r = \xi |t|^{\bar{n}} \tag{31}$$

where time is negative and increasing before collapse ($t = 0$ at collapse). Equation (31) is used in a similarity argument to reduce the continuity, momentum, and energy equations for a perfect, inviscid, non-heat conducting gas to ordinary differential phase-plane equations. The actual details of this reduction and the integrations are too lengthy to reproduce here, but a complete description is found in GUDERLY (1942).

Physically, we think of an infinitely strong shock wave contracting into an undisturbed uniform medium of density ρ_0 and zero pressure (a standard approximation). The jump conditions across the shock are

$$\begin{aligned} \rho_1/\rho_0 &= (\gamma + 1)/(\gamma - 1) \\ u_1 &= 2\bar{U}/(\gamma + 1) \\ p_1 &= 2\rho_0\bar{U}^2/(\gamma + 1) \end{aligned} \tag{32}$$

where ()₁ denotes conditions behind the shock, γ is the ratio of specific heats, and \bar{U} is the frontal velocity

$$\bar{U} = dr/dt = -\bar{n}\xi^{1/\bar{n}}r^{1-1/\bar{n}}. \tag{33}$$

After collapse, a new discontinuity is generated which expands from the center. Increasing values of ρ and p are found behind the contracting front, while relaxing profiles are seen behind the expanding front.

A detailed study of the phase-plane is necessary in order to carry out the integrations subject to the initial conditions (32). This is possible for the spherical problem and $\gamma = \frac{5}{3}$ only if the exponent in (31) is 0.688377. The resulting curves of $p/\rho_0\bar{U}^2$ and ρ/ρ_0 as functions of $t/|t_0|$ are shown in Figs. 11 and 12 (Guderly's results are for $\gamma = \frac{7}{5}$) where $|t_0|$ is the time at which the imploding shock first passes the observation point r^* . For all positions, the shock passes to the origin at $t/|t_0| = 0$ and the reflected discontinuity again reaches r^* at $t/|t_0| = 1.59$.

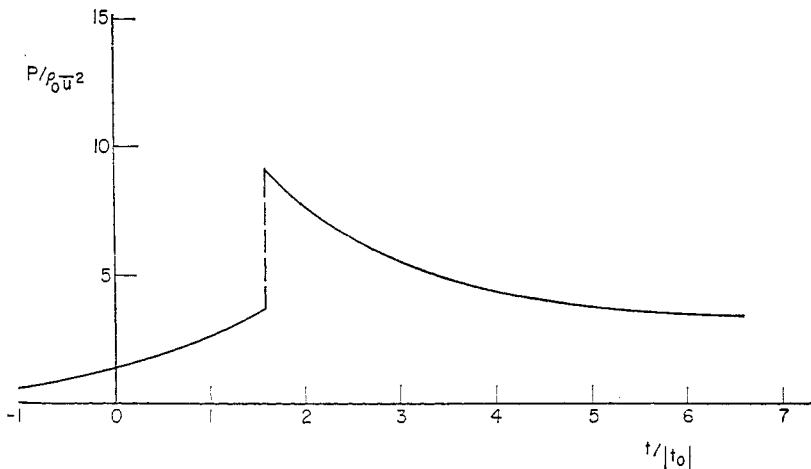


FIG. 11.—Normalized pressure as a function of $t/|t_0|$ at the observation point r^* from the shock dynamics analysis.

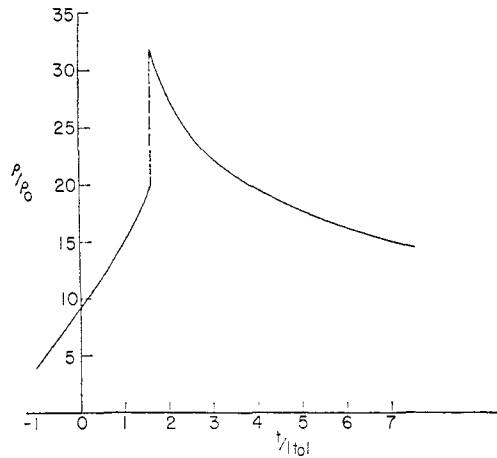


FIG. 12.—Normalized density as a function of $t/|t_0|$ at the observation point r^* from the shock dynamics analysis.

To construct the neutron production-shock speed parameter curve, we select values of ξ and calculate the corresponding values of $|t_0|$ and \bar{U} from equations (31) and (33). The plasma is divided into shells of thickness Δr with mean radius r^* , and ρ^*/ρ_0 and $p^*/\rho_0 \bar{U}^2$ are selected from the tabular solutions of the phase-plane equations. If we now assume that the medium into which the shock propagates is an equal mixture of ions and electrons, the ion densities and temperatures become

$$n = n^+ = n_0 \rho^*/\rho \quad T^+ = (p^*/\rho_0 \bar{U}^2)(\rho_0/\rho^*)(m^+/2k)\bar{U}^2. \quad (34)$$

The last factor of 2 arises from the relations

$$\rho_0 = n_0(m^- + m^+) = 2n_0 m_a, \quad m_a = (m^+ + m^-)/2 \simeq m^+/2 \quad (35)$$

where m_a is the averaged particle mass of the ion-electron fluid. n and T^+ are substituted into equation (21) for D - D reactions and the results are integrated over time and space to obtain the net neutron production curve of Fig. 13.

We can calculate a value of ξ for each of the shock dominated cases by tabulating the position of the front, defined as the location of $(n_{\max} + n_0)/2$ as a function of time. Since this time is measured positively from the start of the laser pulse, equation (31) is rewritten as

$$r = \xi |t - t_c|^{0.688277} \quad (36)$$

where t_c is the time of collapse. A best fit value of ξ is found and these are listed in column 8 of Table 1.

Total neutron production in the cases run to completion has been indicated in Fig. 13, and the agreement with the model curve is excellent. This result can be interpreted as follows: the laser pulse creates a strong thermal disturbance which in turn initiates a strong shock characterized by the parameter ξ . Once the shock reaches full strength, the laser and thermal effects are no longer important compared with the convergence. Since a purely hydrodynamic model, without transport processes, can predict the output to such a high degree of accuracy, we can conclude that the attenuation of the wave by viscous effects must be negligible and that the increased electron temperatures behind the shock (due to thermal transport of laser energy) has a negligible effect on ion temperature.

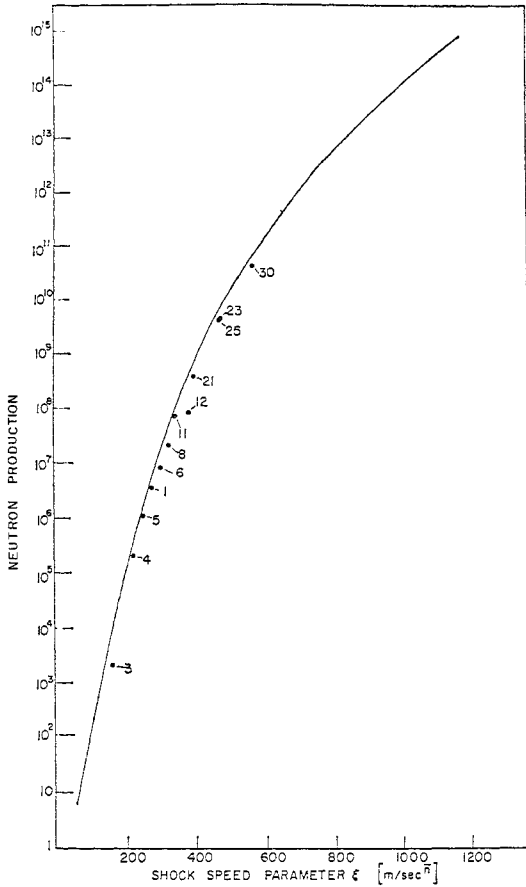


FIG. 13.—Neutron production from the shock dynamics analysis model as a function of the shock parameter ξ . Comparison cases from Table 1 are indicated.

7. ANALYSIS OF NEUTRON PRODUCTION

We use the results of the last section to explain the behavior of the neutron production curve in Fig. 8. Figure 14 shows the shock speed parameter as a function of absorbed energy for various core radii (note again that these curves are independent of the absorption mechanism and the tail thickness). The value of ξ associated with a shock depends both on its radius and on its velocity when it reaches full strength as seen by solving equation (33)

$$\xi = (-\hat{U}/\bar{n})^{\bar{n}} r^{1-\bar{n}} \tag{37}$$

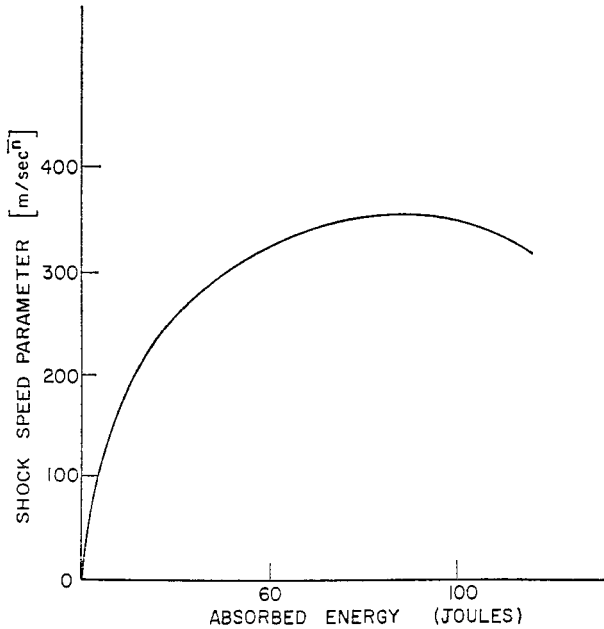
where $\hat{}$ denotes conditions just at full strength. At first there is an increase of ξ with E_a because the thermal front decays into a shock wave at increasingly higher sonic velocities. Although these sonic velocities, and, by convergence, \hat{U} , continue to increase with E_a , the thermal effects become more persistent, and the point of decay is eventually postponed long enough to decrease both \hat{r} and ξ .

Since neutron production varies monotonically with the shock speed parameter in Fig. 13, and since ξ shows a maximum as a function of E_a in Fig. 14, we expect the neutron production curve to peak in the shock dominated region of Fig. 8. Further

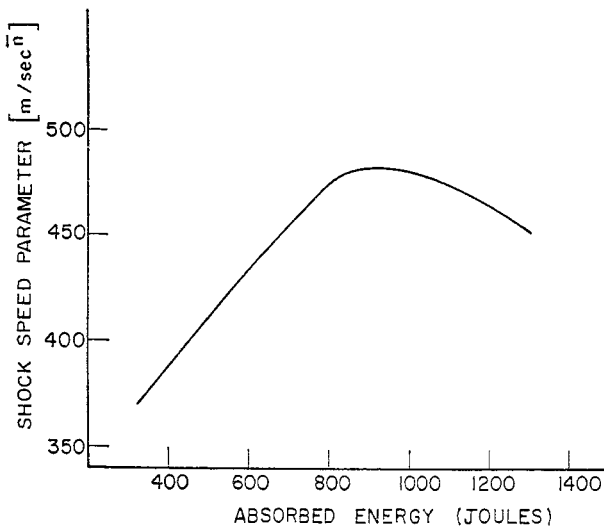
increases of E_a lead to thermally dominated behavior where either the transition is delayed so long that the shock cannot reach full strength or the transition cannot occur at all. The continued negative slope of the neutron production curve can be understood from the following simple arguments.

If we substitute V_T from equation (13) into (17), we obtain

$$\bar{U} \simeq (T)^{-3/2} \quad (38)$$



(a)



(b)

FIG. 14.—Shock speed parameter as a function of absorbed energy from the experimental data (a) $r_c = 100 \mu$, (b) $r_c = 200 \mu$, (c) $r_c = 300 \mu$.

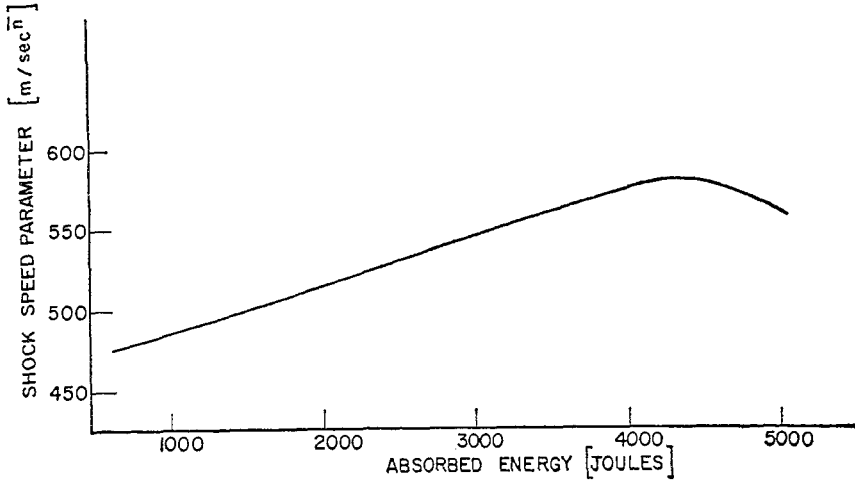


FIG. 14 (c)

This indicates that the velocity behind the front decreases with increasing absorbed energy and these decreased velocities lead to reduced density enhancements by convergence after the front has reached the center. Figure 15 confirms these results. Case 15, which absorbs 177.6 J shows greater maximum density perturbations than case 17 which absorbs 208.5 J. The corresponding average ion temperatures appear in Fig. 16. Lower values for case 17 can be understood from equation (11) where lower densities and higher electron temperatures lead to poorer energy accommodation between the species. Both the lower density and the lower ion temperature lead to lower neutron production from equation (21).

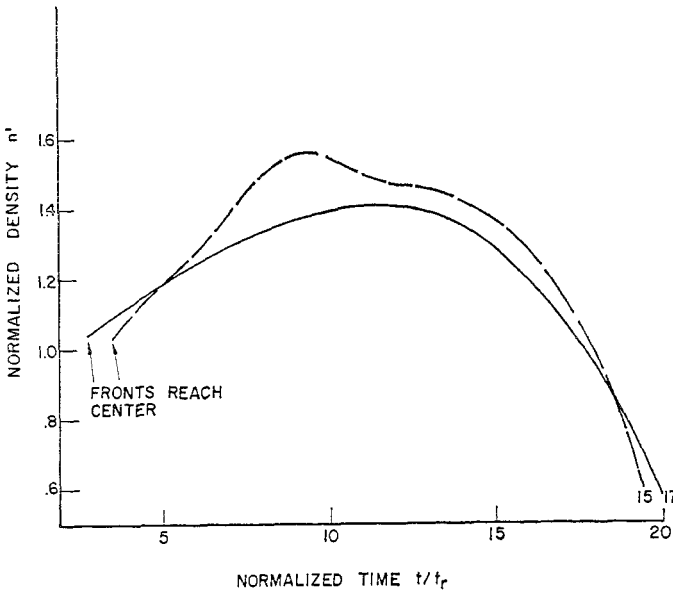


FIG. 15.—Maximum values of the normalized density as a function of normalized time for cases #15 and #17.

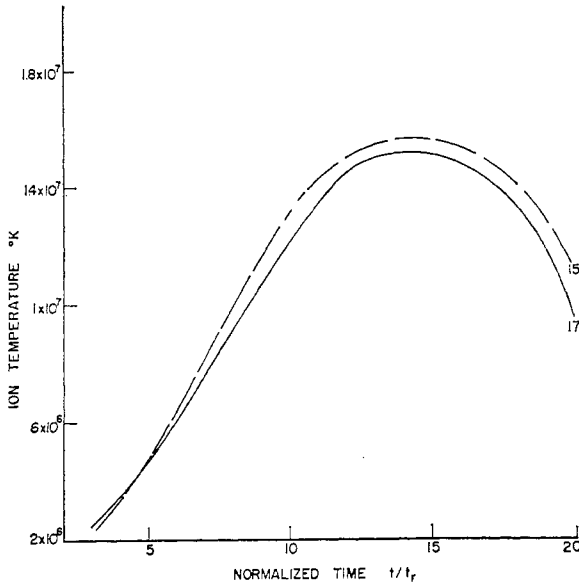


FIG. 16.—Averaged ion temperature as a function of normalized time for cases #15 and #17.

8. SCALE ANALYSIS OF ξ

Let E_{a1} and E_{a2} be the absorbed energies in two plasmas with core radii r_{c1} and r_{c2} , and let $\bar{r}'_1 = \bar{r}_1/r_{c1}$ and $\bar{r}'_2 = \bar{r}_2/r_{c2}$ be the non-dimensional radii at which the respective heat fronts decay to shock fronts. The corresponding sonic velocities would then be in the ratios

$$U_{a2}:U_{a1} = (T_2^-)^{1/2}:(T_1^-)^{1/2} = [E_{a2}/r_{c2}^3(1 - \bar{r}'_2{}^3)]^{1/2} : [E_{a1}/r_{c1}^3(1 - \bar{r}'_1{}^3)]^{1/2}. \quad (39)$$

Since the results of Section 3 require that $U_{a1} = U_{a2}$, the proportionality

$$E_{a1}:E_{a2} = r_{c1}^3:r_{c2}^3 \quad (40)$$

reduces equation (39) to $\bar{r}'_1 = \bar{r}'_2$.

We can obtain a relation between the density, frontal velocity and radius at the transition from thermal to shock behavior and those at full strength by following the motion of the front. Ignoring changes purely with respect to time, the continuity equation (14) gives

$$\hat{\rho}\hat{U}\hat{r}'^2 = \bar{\rho}U_a\bar{r}'^2 \quad (41)$$

where $\bar{\rho}$ is equal to the original solid density and, by definition, $\hat{\rho} = 4\bar{\rho}$. Since U_a , \bar{r} , $\bar{\rho}$, and $\hat{\rho}$ are the same for any two plasmas, equation (41) leads to

$$\hat{U}_1\hat{r}'_1{}^2 = \hat{U}_2\hat{r}'_2{}^2. \quad (42)$$

Because the normal shock relations hold locally at each point of a curved shock, there exists a unique relation between \hat{U} and $\hat{\rho}$ just up to the time at which we apply our full strength assumptions (i.e. before we impose equations (32)). The fact that $\hat{\rho}$ is the same for any two plasmas then implies that $\hat{U}_1 = \hat{U}_2$ and, from (42), $\hat{r}'_1 = \hat{r}'_2$.

The ratio of shock speed parameters for two plasmas is formed from equation (37)

$$\frac{\xi_2}{\xi_1} = \left(\frac{r_{c2}}{r_{c1}}\right)^{1-\bar{n}} \left(\frac{\hat{r}'_2}{\hat{r}'_1}\right)^{1-\bar{n}} \left(\frac{\hat{U}_2}{\hat{U}_1}\right)^{\bar{n}} \tag{43}$$

Using the results obtained above and $n = 0.688377$, equation (43) reduces to

$$\frac{\xi_2}{\xi_1} = \left(\frac{r_{c2}}{r_{c1}}\right)^{0.311623} \tag{44}$$

Figure 17 shows the curves of Fig. 14 reduced to a 100 μ base curve through equations (40) and (44) (e.g. for case 18 with $r_c = 200 \mu$, the absorbed energy and ξ are reduced by 2^3 and $2^{0.311623}$, respectively). Excellent agreement is seen on the common portions of the curve.

A slight modification of the similarity analysis of ZELDOVICH and RAIZER (1966) shows that as long as (40) holds, the sudden addition of heat at the surface of a sphere leads to $V_{T2}:V_{T1} = r_{c1}:r_{c2}$. If $V_{T2} > V_{T1}$, this requires $\hat{r}'_2 > \hat{r}'_1$ since a smaller value of V_T means faster decay from the thermal to the shock mode. We can anticipate, then, that there will be cases for which (40) holds, but where the smaller plasma will be thermally dominated while the larger will be shock dominated. Equation (44) can therefore be expected to hold only as long as $\xi \leq \xi_{max}$ for both plasmas.

Although we do not have the data to extend this curve, the scalings (40) and (44) would allow us to run a single series of experiments for a large particle, say one with $r_c = 2000 \mu$, and then to calculate the corresponding E_a and ξ for smaller plasmas. The absorbed energy reduced by $(r_c/100 \mu)^3$, at which maximum ξ 's occur are shown in Fig. 18 for core radii of 100, 200 and 300 μ . If this linear relation holds for larger r_c , we can then determine the optimum shock dominated neutron output for any plasma with $r_c \leq 2000$.

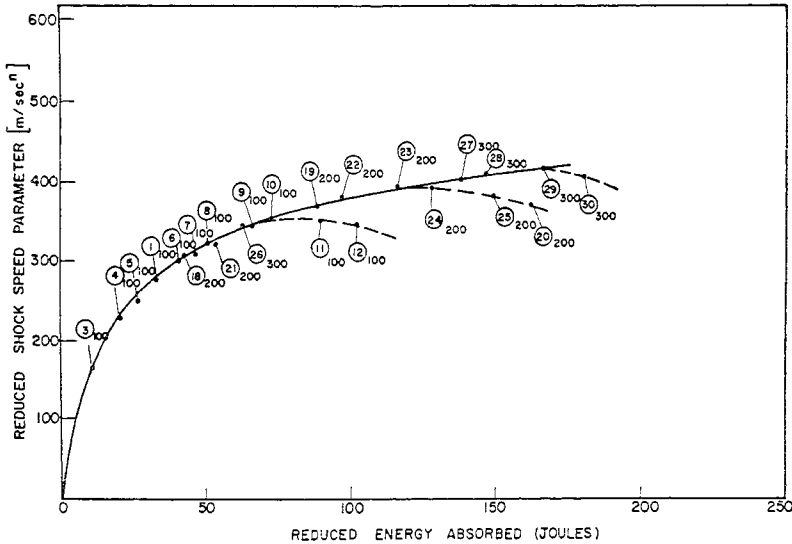


FIG. 17.—Shock speed parameter as a function of absorbed energy. ξ and E_a for the $r_c = 200 \mu$ and $r_c = 300 \mu$ cases have been reduced as explained in Section 8. All points have been numbered as in Table 1 and r_c , in microns, has been indicated.

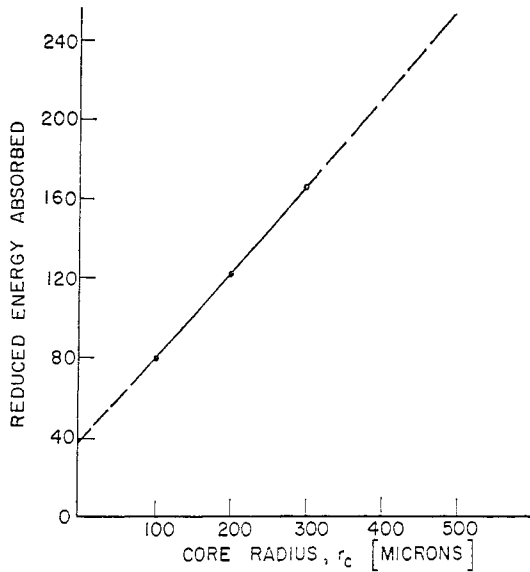


FIG. 18.—Reduced absorbed energy at maximum ξ as a function of r_c showing the linear dependence for the three data points.

Acknowledgement—This research was carried out in the Laboratory for Laser Energetics with a contract from the National Science Foundation, GK-18578. Supplemental computing funds were supplied under the National Science Foundation Grant GJ-828.

REFERENCES

- ARTSIMOVICH L. A. (1962) *Controlled Thermonuclear Reactions*, Gordon and Breach, New York.
 DAWSON J. (1964) *Phys. Fluids* **7**, 981.
 DAWSON J. and OBERMAN C. (1962) *Phys. Fluids* **5**, 517.
 FADER W. (1968) *Phys. Fluids* **11**, 2200.
 GENTRY R., MARTIN R. and DALY B. (1966) *J. Comp. Phys.* **1**, 87.
 GOLDMAN E. (1971) University of Rochester, Laboratory for Laser Energetics, Report No. 6.
 GUDERLY G. (1942) *Luftfahrtforschung* **19**, 302 (Trans: C. Wittliff).
 HAUGHT A. and POLK D. (1970) *Phys. Fluids* **13**, 2825.
 KAW P. and DAWSON J. (1969) Princeton University Plasma Physics Report MATT-676.
 LEISING W., McIVER J. and LUBIN M. (1972) University of Rochester, Laboratory for Laser Energetics, Report No. 11.
 LUBIN M., GOLDMAN E. and YUAN K. (1971) University of Rochester, Laboratory for Laser Energetics, Report No. 5.
 MEAD S. (1970) *Phys. Fluids* **13**, 1510.
 ZELDOVICH, Y. and RAIZER Y. (1966) *Physics of Shock Waves and High-Temperature Hydrodynamic Phenomena*, Vol. II, Academic Press, New York.